Postprint of: Jha A.K., Lamecki A., Mrozowski M., Bozzi M., "A Microwave Sensor with Operating Band Selection to Detect Rotation and Proximity in the Rapid Prototyping Industry," in IEEE Transactions on Industrial Electronics (2020)
DOI: 10.1109/TIE.2020.2965464

A Microwave Sensor with Operating Band Selection to Detect Rotation and Proximity in the Rapid Prototyping Industry

Abhishek Kumar Jha, *Member, IEEE*, Adam Lamecki, *Senior Member, IEEE*, Michal Mrozowski, *Fellow, IEEE,* and Maurizio Bozzi, *Fellow, IEEE*

***Abstract*—This paper presents a novel sensor for detecting and measuring angular rotation and proximity, intended for rapid prototyping machines. The sensor is based on a complementary split-ring resonator (CSRR) driven by a conductor-backed coplanar waveguide (CBCPW). The sensor has a planar topology, which makes it simple and cost-effective to produce and accurate in measuring both physical quantities. The sensor has two components, a rotor and a stator: the first of these (the CSRR) can rotate around its axis and translate along the plane normal to the ground of the CBCPW. A detailed theoretical and numerical analysis, along with a circuit model, of the unique sensor design is presented. The proposed sensor exhibits linear response for measuring angular rotation and proximity in the range of 30–60 degrees and 0–200 µm. Another distinctive feature of the rotation and proximity sensor is the wide frequency band of applicability, which is an integral part of its novel design and is implemented through various dielectric material loadings on the CSRR. In the prototype of the proposed device, the stator (CBCPW) was fabricated on a 0.508-mm-thick RF-35 substrate, while the CSRR-based rotor was fabricated on TLY-5 and RF-35 substrates. The angular rotation, the proximity, the operating band selection and the sensitivity were measured using a vector network analyzer, and were found to be good matches to the simulated and theoretical results.**

***Index Terms*—Additive manufacturing, conductor-backed coplanar waveguide, dielectric constant, material characterization, microwave planar sensor, proximity sensor, rapid prototyping industry, rotation sensor.**

This work was supported in part by the "EDISOn - Electromagnetic Design of flexIbleSensOrs" project, agreement no POIR.04.04.00-00-1DC3/16-00 date 06.12.2016 r., which is carried out within the TEAM-TECH programme of the Foundation for Polish Science co-financed by the European Union under the European Regional Development Fund, Smart Growth Operational Programme 2014–2020. *(Corresponding author: Abhishek Kumar Jha.)*

A. K. Jha and M. Mrozowski are with the Department of Microwave and Antenna Engineering, ETI Faculty, Gdańsk University of Technology, 80-233 Gdańsk, Poland (e-mail: abhishek.jha@pg.edu.pl, mim@pg.edu.pl).

A. Lamecki is with the Department of Microwave and Antenna Engineering, ETI Faculty, Gdańsk University of Technology, 80-233 Gdańsk, Poland, and also with EM Invent, Trzy Lipy 3, 80-172 Gdańsk, Poland and (e-mail: adam.lamecki@eminvent.com).

M. Bozzi is with the Department of Electrical, Computer and Biomedical Engineering, University of Pavia, 27100 Pavia, Italy (e-mail: maurizio.bozzi@unipv.it).

I. INTRODUCTION

THE FUTURE OF RAPID PROTOTYPING MACHINES, especially in the electronics industry (including aerospace, defense, and healthcare), depends on the precision obtained in calibration and fabrication. In devices operating in the microwave, THz, and optical ranges, precision is usually sought on the submicrometer scale. The distributed circuits used in radio frequency (RF) usually have thicknesses of substrate and metal layer in millimeters and micrometers, respectively. In line with the definition of penetration depth and the power handling capacity at higher frequencies, the thicknesses of the substrates and metal layers can decrease further to the micrometer and nanometer scales, respectively. Handling and fabricating distributed circuits at higher frequencies using the standard fabrication protocols becomes complex. This is one reason that low-cost fabrication of millimeter-wave and THz devices is quite difficult given the allowable surface roughness and precision. Most low-cost rapid prototyping machines (whether additive or subtractive) and computer numerical control (CNC) machines have problems in precisely calibrating their z-axis (height) [1]–[2], which leads to inaccurate prototypes, which are usually inhomogeneous in thickness. Z-axis calibration becomes more important in the design of multilayer printed circuit boards, where etching or adding an extra layer can create air gaps that may result in the severing of interlayer connections [3]–[4]. Additionally, precise control over the rotation of prototyping tools can be very helpful in controlling speed and position. Angular rotation and control become more important in the fabrication of 3D devices and components when working with different kinds of materials in prototyping industries [5].

Being able to detect rotation is one of the more important requirements in the automation industry; this is why rotation sensors based on capacitive [5], optical [6], and magnetic [7] principles are readily available. Recently, an angular displacement sensor based on the magnetic equivalent loop method is proposed with a shared magnetic field for higher accuracy [8]. A rotation monitoring system based on the wireless power transfer using transmitter and receiver coils equipped with class-E power amplifier and multiple motors is proposed in [9]. The rotation monitoring system is proposed for the prosthetic hands to measure in the angular rotation

from −45° to +45°, where the power transfer efficiency records a minimum value for ±45° at a distance of 30 mm. A magnetoresistive sensor combined with permanent magnets is proposed to measure a complete rotation angle with low error for the high amplitude of magnetic field ranging from 100 Oe to over 1 kOe [10].

Proximity detection is another important parameter essential in the automation industry, including mobile communications. Recently, proximity sensors based on capacitive microelectromechanical technology [11], dynamic vision-sensing technology [12], received signal strength indicator (RSSI) [13], laser technology [14], and have been described in the literature. Recently, a proximity sensor based on parallel plate capacitance [15], infrared technology [16], ultrasonic technology [17], and multi-channel fiber optic technology [18], and microwave technology [19] have also been proposed.

Although the sensors presented in [6]-[10] offer low-error and good dynamic response, they are bulky due to coils, lenses, and magnets. The amount of coils windings in excitation and pickup coils and the weight of the metal in rotor and stator is a matter of inconvenience. The coil or magnet-based rotation sensors are often suitable for low-frequency operation, and the optics-based rotation sensors need regular maintenance as they suffer mainly in dirty environments and are quite sensitive to the color or the optical transparency of the target. Similarly, sensors presented in [11]-[18] have their own advantages and drawbacks, e.g., The fiber-based proximity sensors provide an excellent resolution in the nm scale; however, the dynamic range is limited in the mm range. The measurement accuracy of the capacitance type sensor varies depending on the dimension and the ground state of the object or material under test; therefore, a calibration method is essential.

In contrast, the microwave sensor is lightweight as compared with the weight of lenses and magnets used in the optics and magnetic sensors, respectively. Besides the planar technology, the small size is another advantage (the sensor is merely a wavelength long at the operating frequency). Microwave sensors are precise, and suitable for harsh environments, and compare favorably with their mechanical or electronic counterparts thanks to their distributed circuit topology and non-contacting methodology. This is the main reason that some groups of researchers have begun working on microwave-based rotation sensors. Detecting angular displacement using these coplanar sensors is done using various methodologies, including electromagnetic bandgap [20], bisymmetric resonators [21], electric-LC type sensors [22], S-type sensors [23], split-ring resonator (SRR) sensors [24], metamaterial-inspired sensors [25], horn-shaped SRRs [26], complementary split-ring resonator (CSRR) [27] and circularly polarized antennas [28].

However, to the best of our knowledge, a compact microwave sensor that would measure both physical quantities (rotation and proximity)—as generally required in the automation industry—is not to be found in the literature. This paper thus focuses on the development of a planar microwave sensor that can control and measure—rotation and proximity, albeit not a combination of the two.

In this paper, a coplanar microwave sensor for measuring angular rotation and proximity is designed, fabricated, and tested. The sensor is based on a conductor-backed coplanar waveguide (CBCPW) loaded with a complementary split-ring resonator (CSRR), where the CSRR is allowed to rotate around the axis and free to move along the axis of CSRR (Fig. 1). The angular rotation is detected using the cross-coupling between the CBCPW and the CSRR, which varies as the CSRR is rotated. As a result, the effective mutual inductance changes, affecting the resonance. The proximity is detected using the near-field technique. The resonant frequency also changes here, but the change in the resonance of the CSRR is due to the change in the effective capacitance between the transmission line and the CSRR. The theoretical model for calculating the angular rotation and proximity was developed using first principles. The performance of the proposed sensor was checked using numerical simulations, which confirmed that the sensor was a good candidate for measuring both rotation and proximity. Additive manufacturing technology was used to build a fixture that holds the CBCPW and CSRR assembly with a micrometer screw, which can efficiently rotate and move as required with. The measurements were found to be in good agreement with the simulated and calculated data.

This paper is organized as follows: A detailed illustration of the design methodology of the proposed sensor is given in Section II. Section III discusses the multiband rotation sensor, while section IV describes the multiband proximity sensor. Section V describes the measurement carried out using the sensor, section VI discusses the outcomes, and section VII summarizes the conclusions.

II. DESIGN OF THE ROTATION SENSOR

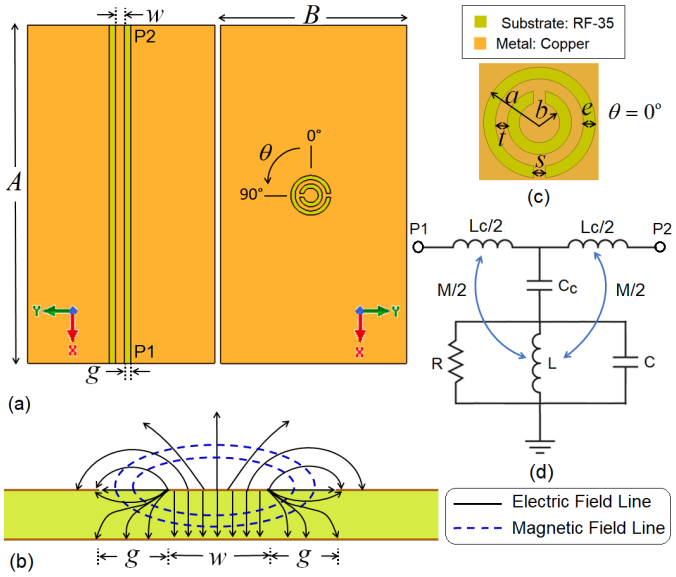

Fig. 1. (*a*) Top and bottom plane of the CSRR coupled conductor backed CPW, (*b*) electric and magnetic field lines of the CPW, (*c*) zoomed view of the CSRR with design parameters, (*d*) an equivalent circuit representation of the rotatable CSRR with cross-coupling.

A. Theoretical Design

The sensor was designed using CBCPW technology, which offers better control of ratio between the gap g and the line-width w (Fig. 1) compared to standard CPW technology excited using a 50-Ω SMA connector. CBCPW also provides more mechanical strength and is well-suited to the narrow-band characteristics of a resonator sensor. Before considering the practical design, we investigate a structure consisting of a complementary split-ring resonator etched on the ground plane at the center of the CBCPW, as shown in Fig. 1(a). The CSRR is usually etched on the ground plane, keeping the slit of the CSRR (whose thickness is s) transverse to the CBCPW (θ = 90°). In this configuration, where the CSRR is symmetric to port P1 and port P2, the electric field lines of the CBCPW normal to the ground plane (as shown in Fig. 1(b)) excite the CSRR. However, a small axial rotation from θ = 90° (clockwise or counterclockwise) perturbs the symmetry of the CSRR, due to the asymmetric positioning of slits with respect to P1 and P2. In the asymmetric condition, the slits of the CSRR, which were parallel to the magnetic field lines of the CPW at θ = 90°, now make a finite angle with the magnetic field lines of CBCPW. At θ = 0° (as shown in Fig. 1(c)), the linkage of the magnetic field lines of the CBCPW with the slits of CSRR reaches its maximum value. From circuit theory, this induced effect can be explained by the mutual induction between the inductances of the CSRR (L) and the CBCPW (L_C), as shown in Fig. 1(d) [29]. The mutual inductance can be given as M = $k\sqrt{LL_c}$, where k is the coefficient of mutual induction, which depends on the axial rotation of the CSRR. C and C_c represent the effective capacitance of the CSRR and the capacitance due to the electric coupling of the CSRR with the CBCPW, respectively.

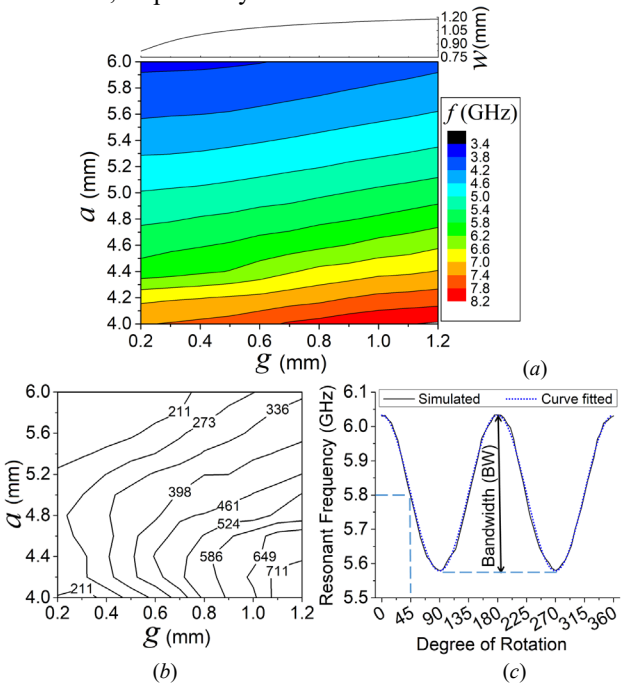

Fig. 2. (a) Color-filled contour plot of the resonant frequency; (b) contour lines labeled with bandwidth (in MHz) with respect to the change in a and g; and (c) the locus of resonant frequency for one complete rotation of the CSRR

At first, the CSRR fed with the CBCPW (as shown in Fig. 1) is designed on RF-35 substrate with a dielectric constant ε_s = 3.5, a loss tangent tan δ = 0.0018, height h_s = 0.508 mm, and copper thickness T = 18 μm. The scattering coefficients are numerically computed for various combinations of the design parameters, where the resonant frequency of CSRR is estimated from the transmission coefficient data. To determine the characteristics of the CSRR under rotation—namely, the resonant frequency f, the bandwidth BW, and angular rotation—the CSRR is rotated from θ = 0° to 360°; the results are given in Fig. 2. Since CBCPW technology offers flexibility in designing a 50-Ω transmission with adequate combinations of g and w values, f and BW are also calculated for various combinations of g and w. The dominant parameter in controlling the resonant frequency of CSRR, its outer radius a [Fig. 1(c)], is varied to obtain the desired characteristics, while keeping e = s = t = 0.5 mm. To determine the design parameters at the central frequency of operation, the CSRR is simulated at θ = 45°; the results are given in Fig. 2(a). In Fig. 2(a), the value of f increases as a decreases; however, it is interesting to note that, for a fixed value of a, the value of f increases as g and w increase. From Fig. 2(a), it is evident that the design of the CSRR-based sensor on CBCPW technology grants more degrees of freedom than microstrip technology. To feed the CBCPW directly from a 50-Ω subminiature A (SMA) connector, and to obtain the resonant frequency at 5.8 GHz on the ISM band, the value of g was taken as 0.7 mm, resulting in w = 1.1 mm and a = 4.7 mm. A similar observation was made for BW; Fig. 2(b) shows that increasing g and decreasing a gives a larger BW. Fig. 2(c) shows that the simulated locus of f is nearly sinusoidal with respect to θ, and a 450 MHz BW is achieved at the 5.8 GHz in the ISM band. It may be noted that, with the help of additional circuitry capable of envelope detection, the angular velocity with respect to time can be estimated. However, the aim of this paper is to detect only the axial rotation and the proximity.

B. Practical Design

The CSRR should be free to rotate around its axis if the design of the rotatable sensor is to be practical. A concentric gap of thickness t_g is thus etched out around the CSRR at a distance t_c from the outer ring [Fig. 3(a)]. An equivalent circuit of the rotatable CSRR-based sensor cross-coupled to the CBCPW is given in Fig. 3(b), where C_g represents the capacitance between the gap t_g of the two concentric cylinders of thickness t [30], whereas the equivalent inductance of the CSRR, L_m, which considers the cross-coupling effect, can be given as

$$C_g = 2\pi\varepsilon_{eff} t\left[\ln\left(1+\frac{t_g}{b+t_c}\right)\right]^{-1};\quad L_m = L - k\sqrt{LL_c} \tag{1}$$

where ε_{eff} is the effective permittivity. The resonant frequency of the rotatable CSRR-based sensor can be given as

$$f^{-2} = 4\pi^2\left(\frac{CC_c + CC_g + C_cC_g}{C_c + C_g}\right)L_m \tag{2}$$

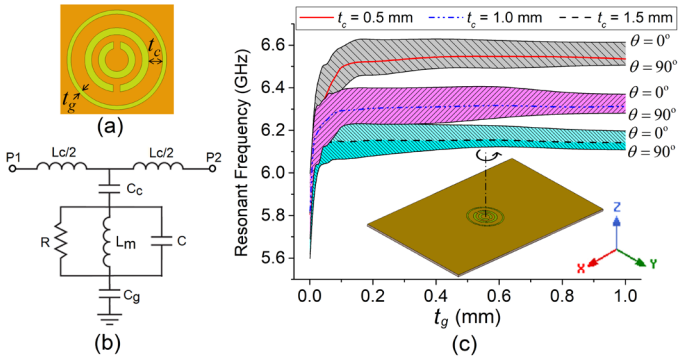

Fig. 3. (*a*) CSRR with a concentric gap for free rotation around the axis; (*b*) Equivalent circuit representation; (*c*) plot of resonant frequency at $\theta = 45°$ and bandwidth of the CSRR sensor with respect to variation in t_c and t_g, and 3D structural view indicating the location and operation of the rotor in the inset.

A parametric numerical study was performed to check the effects of t_c and t_g on the f and BW of the rotation sensor. From the results in Fig. 3(*c*), it can be observed that t_g strongly affects the resonant frequency of CSRR for values smaller than 0.1 mm. For t_g > 0.1 mm, the resonant frequency of CSRR mostly depends on the value of t_c. This particular response can be explained from (2), where the logarithmic variation in C_g dominates at smaller values of t_g. It should be noted that BW is lower at higher values of t_g and t_c—that is, t_g changing from 0 to 1 mm results in BW decreasing; BW from 450 MHz to 91 MHz, 85 MHz, and 81 MHz for t_c = 0.5 mm, 1 mm, and 1.5 mm, respectively. It is interesting to note from Fig. 3 that, for t_c = 1 mm, the value of the resonant frequency at $\theta = 45°$ appears to be the center frequency of BW up to t_g = 0.4 mm. The value of t_c is taken so as to achieve the maximum BW (170 MHz) with the smallest machinable dimension (= 0.3 mm), in order to result in a practical design. The design parameters of the CBCPW-driven CSRR-based rotation sensor is given in Table I.

TABLE I.
DESIGN PARAMETERS OF THE ROTATION SENSOR AND THEIR VALUES

Parameters	*A*	*B*	*w*	*g*	*a*	*b*	*e*	*t*	*s*	t_c	t_g
Values (mm)	40	25	1.1	0.7	4.7	3.2	0.5	0.5	0.5	1	0.3

C. Extraction of Circuit Parameter

First, the CSRR was placed inside an air-filled rectangular cavity (10 mm × 10 mm × 10 mm), operating in TE_{101} mode at 21.21 GHz (much higher than the fundamental frequency of the CSRR), and eigenmode analysis was performed using HFSS software. The results are displayed in Figs. 4(*a*) and (*b*), which show the electric and magnetic fields of the fundamental mode, along with the unloaded resonant frequency f_0 ~ 10.65 GHz and the quality factor Q_0 ~ 483. Later, the CSRR was excited using CBCPW without a gap (t_g = 0 mm) and with a gap (t_g = 0.3 mm), as discussed earlier and shown in Figs. 4(*c*) and (*d*); the resonant frequencies were recorded as f_L = 5.64 GHz and f_{Lg} = 6.22 GHz, respectively. Based on the simulation data for θ = 90°, the value of the lumped circuit parameters were calculated using (3)–(6). Since there were five unknowns and four equations, a unique solution of the nonlinear system of equations (3)–(6) was achieved, using the condition that the loaded quality factors calculated by numerical simulation and the circuit approach were the same.

It is interesting to observe from Fig. 4(*c*) and (*d*) that, although the overall size of the CSRR with a gap of t_g increases, the resonant frequency increases above that seen in the CSRR without a gap. Further, the confinement of the electric field is more pronounced in the CSRR with the gap, mainly on account of the increase in the quality factor. The CSRR with gap may thus also be an interesting design for high-frequency applications, while keeping the overall design relatively large.

$$f_0^{-2} = 4\pi^2 LC \quad (3); \qquad Q_0 = \frac{R}{2\pi f_0 L} \quad (4)$$

$$f_L^{-2} = 4\pi^2 L(C + C_c) \quad (5); \qquad f_{Lg}^{-2} = 4\pi^2 L\left(C + \frac{C_c C_g}{C_c + C_g}\right) \quad (6)$$

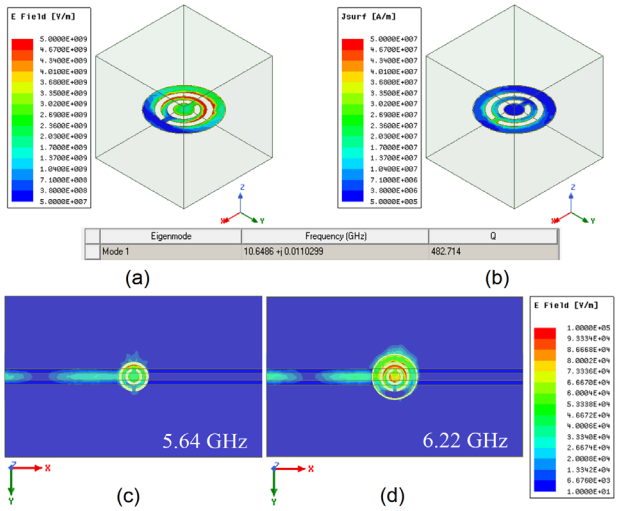

Fig. 4. (*a*) Electric field and (*b*) magnetic field of the CSRR using eigenmode analysis; Electric fields of the CSRR (*c*) without a gap and (*d*) with a gap, using frequency domain analysis.

The transmission coefficients calculated using the numerical simulation and circuit approaches are plotted in Fig. 5(*a*), and the extracted circuit parameters for the proposed CSRR at θ = 90 are given as C = 0.043 pF, C_c = 0.109 pF, C_g = 0.335 pF, L = 5.25 nH, R = 169.68 kΩ, and L_c = 0.8 nH.

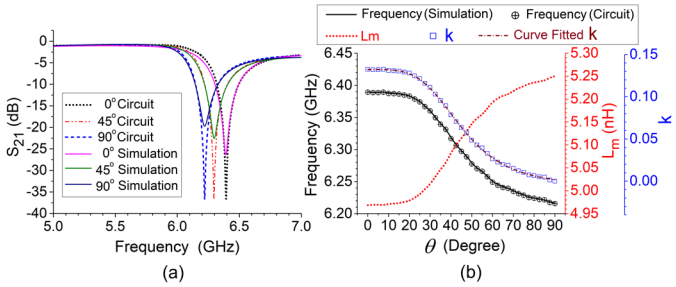

Fig. 5. (*a*) Comparison of transmission coefficients obtained from the numerical and circuit approaches, (*b*) response of the rotation sensor over an angular span of 90° with the values of their variable parameters.

It can be observed from Fig. 5(*a*) that the loaded quality factor of the sensor increased as θ decreased from 90°, which is equivalent to a drop in the value of L of a parallel resonator

due to mutual induction from the CBCPW inductance. A detailed observation was carried out for a fine angular step of 2.5°. The results in Fig. 5(*b*) show that the coefficient of coupling k increased from 0 to 0.13, while the value of L_m decreased from 5.25 nH to 4.97 nH as the sensor was rotated from $\theta = 90°$ to 0°. To represent the angular rotation in terms of mutual induction, the calculated value of k was used with the dose–response curve fitting algorithm, giving an excellent fit with Pearson's chi-squared test value of 9.1×10^{-7}. The relation can be given as

$$k = A_2 + \left(A_1 - A_2\right) \Big/ \left[1 + \left(\theta / A_0\right)^y\right] \qquad \forall \theta = \left[0^o, 90^o\right] \tag{7}$$

where A_0, A_1, A_2, and y are constants with values 45.39, 1.32×10^{-1}, -6.73×10^{-3}, and 4, respectively. It can be seen from Fig. 5(*b*) that the proposed rotation sensor has a linear relation with θ over the broad angular span from 30° to 60°. Since linearity is required for practical instrumentation reasons, a linear relation between k and θ (in degree) was developed as

$$k = B_0 + B_1\theta \qquad \forall \theta = \left[30^o, 60^o\right] \tag{8}$$

where the values of B_0 and B_1 are 1.94×10^{-1} and -2.84×10^{-3}, respectively. Since most practical sensors in various industrial applications require multiband operation, our rotation sensor offers band selectivity, which is explained in the next section.

III. OPERATING BAND-SELECTION FOR THE ROTATION SENSOR

In the proposed design, band selectivity is introduced by separating the CSRR from the substrate, while etching it on a separate dielectric puck, as shown in Fig. 6(a). In this design, the dielectric material loading on the CSRR introduces another degree of freedom, as it affects the resonant frequency and the BW. By adopting dielectric pucks of different heights, and permittivities, various bands can be selected. The dielectric puck also increases the mechanical strength and rigidity of the CSRR, to meet the requirements of the rapid prototyping industry. Since the sensor consists of two parts, the movable part (the CSRR on a puck) is called the rotor, while the substrate (the CBCPW*)* is called the stator. A 3D structure of the assembled stator and rotor is shown in Fig. 6(b).

The introduction of dielectric support can be accounted for in a circuit model by adding a capacitance C_m in parallel with the capacitance C of the resonator, as shown in Fig. 6(*c*). The resonant frequency of the rotation sensor can now be given as

$$f_r = \left[2\pi\sqrt{\left(L - k\sqrt{LL_c}\right)\left(C + C_m + \left(C_c^{-1} + C_g^{-1}\right)^{-1}\right)}\right]^{-1} \tag{9}$$

In order to obtain the resonant frequency and BW from (9), we need the values of C_m with respect to the various design parameters of the dielectric puck. A generalized theoretical model is thus developed here to calculate the values of C_m. The additional capacitance depends on the design parameters of the CSRR and type of material loading. The dielectric puck is assumed to be a dielectric substrate of finite thickness and diameter. To quantify the effect of the resonant frequency shift when the puck is placed on the CBCPW, the effective capacitance is calculated as in [23]. However, to develop a precise model of C_m, the numerical data obtained by varying the dielectric constant ε_m and the height h_m of the puck, as shown in Fig. 6(*d*), are mapped with the theoretical formula [31]. The numerical data of C_m is obtained for the rotor at $\theta =$ 90 —i.e., when $k = 0$. The generalized theoretical model of C_m can be given as

$$C_m\left(\mathrm{pF}\right) = 2\pi a\varepsilon_0\left[m\frac{\mathrm{K}\left(k_a\right)}{\mathrm{K}\left(k_a'\right)} + n\sum_{i=m,s}\left(\varepsilon_i - 1\right)\frac{\mathrm{K}\left(k_i\right)}{\mathrm{K}\left(k_i'\right)}\right] - \mathrm{N} \tag{10}$$

$$k_a = \frac{t}{t+2e};\quad k_{m,s} = \frac{\sinh\left(\pi e/4h_{m,s}\right)}{\sinh\left[\pi\left(t+2e\right)/4h_{m,s}\right]};\quad k'_{a,m,s} = \sqrt{\left(1-k_{a,m,s}\right)}$$

where K represents the complete elliptic integral of the first kind, m, n, and N are arbitrary constants with values 1.22×10^{-1}, 8×10^{-1} and 1.72×10^{-1}, respectively. To determine the values of these constants, a curve-fitting algorithm was used with the simulated values of C_m derived from the resonant frequency that had been determined by full-wave computation. Equation (10) allows the values of C_m to be precisely calculated for $h_m = [0.25$ mm, 1 mm] and $\varepsilon_m = [1, 10]$ with a typical 50% tolerance on nominal dimensions of the CSRR, as given in Table I.

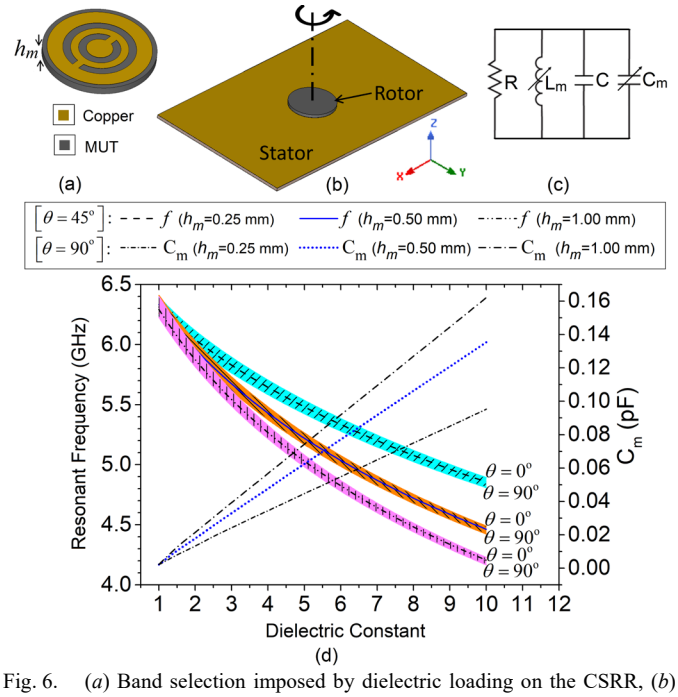

Fig. 6. (*a*) Band selection imposed by dielectric loading on the CSRR, (*b*) 3D structural view indicating the location and operation of the rotor, (*c*) equivalent circuit of the dielectric-loaded CSRR, (*d*) effect of various types of dielectric loading on resonant frequency and BW.

Fig. 6(*d*) shows that the dielectric loading—either in terms of the increase in h_m or ε_m—leads to a decrease in the resonant frequency. However, a variation in ε_m has a much greater effect in controlling the resonant frequency and BW than does h_m, mainly on account of the near-field of the CSRR, which has strong effect only close by; thus, increasing h_m for fixed ε_m does not provide as much control as increasing ε_m for a given

h_m. It can be observed from Fig. 6(*d*) that various dielectric material loadings, ranging from ε_m = 1 to 10, provide a wide range of operating frequency—e.g., the resonating frequency at θ = 90° varies from 6.22 GHz to 4.81 GHz, 4.42 GHz and 4.17 GHz for h_m = 0.25 mm, 0.50 mm, and 1.00 mm, respectively. The BW obtained for various dielectric pucks was also examined in Fig. 6(*d*), where it corresponds to the thickness of the curves. The upper and lower lines of each curve represent the resonant frequency versus the dielectric constant at the angular positions θ = 0° and θ = 90°, respectively, while a curve representing θ = 45° can also be observed between both the curves. The thickness of each curve decreases (as does BW) as the permittivity of the loading material increases. In quantitative terms, as the dielectric constant of the puck ε_m changes from 1 to 10, BW varies from 170 MHz to 82.4 MHz, 65.4 MHz and 59.2 MHz for h_m = 0.25 mm, h_m = 0.50 mm, and h_m = 1.00 mm, respectively.

IV. OPERATING BAND SELECTION FOR THE PROXIMITY SENSOR

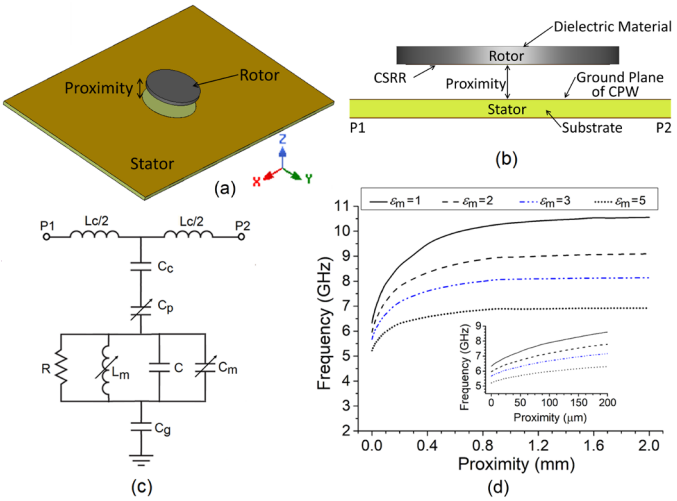

Fig. 7. (*a*) 3D structure of proximity sensor, (*b*) schematic for numerical analysis of proximity using the sensor arrangement, (*c*) equivalent circuit of the tunable proximity sensor, (*d*) response of the dielectric-loaded proximity sensor for h_m = 0.5 mm.

As the previous section illustrated, it is possible to use the rotation sensor over a wide frequency band by using rotors with the same diameter but different material loadings. As band selection is a useful feature, the proposed proximity sensor is examined in terms of the resonant frequency shift for various pucks placed on the movable CSRR part. A 3D structure of the proximity sensor is shown in Fig 7(*a*), while a detailed schematic of the stator and movable part is illustrated in Fig. 7(*b*). The movement of the CSRR, initially placed directly on the ground plane of the CBCPW, is now restricted to the vertical direction, normal to the ground plane of the CBCPW, where θ is arbitrarily fixed to 0°. This particular arrangement introduces a capacitance C_p in series with the coupling capacitance, C_c, as shown in the equivalent circuit diagram of the proximity sensor in Fig. 7(*c*). This capacitance changes as the CSRR moves along the normal to the ground plane of the CPCPW. Though the movement of the rotor away from the ground plane of the CBCPW also alters the value of the gap capacitance C_g, to maintain continuity and simplicity, the value of C_g is considered to be constant, and this effect is jointly expressed in terms of C_p. Since the precision of z-axis calibration and printing requirements of rapid prototyping machines are on the scale of micrometers, the rotor of the proposed sensor is also translated in micrometer steps. A change in resonant frequency is observed, and the calculated data are plotted with respect to the proximity in a range of 2 mm from the ground plane of CBCPW, as shown in Fig. 7(*d*). For multiband operation, the dielectric constant of material loaded on the CSRR is varied over the range of 1 to 5.

It is interesting to note in Fig. 7(*d*) that the sensor is highly sensitive in the unloaded case where ε_m = 1, and attains a resonating frequency of 10.6 GHz for a proximity of 2 mm, which is nearly the same frequency as that obtained by eigenmode analysis of the unloaded rotor in Figs. 4(*a*) and (*b*). This is mainly due to the weak coupling of CSRR through the CBCPW, which almost isolates the CSRR from the external circuitry. This arrangement may be very helpful in calculating the unloaded resonant frequency and the unloaded quality factor of planar resonators. It can be observed from Fig. 7(*d*) that the sensor is highly sensitive close to the CBCPW, and that the response is quite linear up to 200 μm (Fig. 7(*d*) inset).

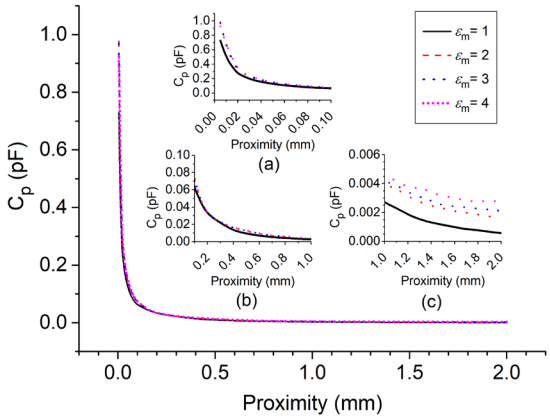

Fig. 8. Plot of capacitance C_p against proximity for various rotors.

To obtain a theoretical model of the resonant frequency, it is important to evaluate the capacitance, C_p. The effective change in C_p due to the change in proximity was thus studied in detail and the results are given in Fig. 8. From the calculated values of C_p against proximity and various dielectric loadings, it can be seen that the response of C_p is similar to the response of a parallel plate capacitor with a variation in the distance between the plates. From Fig. 8, it may be observed that the effect of proximity on C_p dominates over the material loading. To elucidate the dominant behavior of the proximity, the plot is illustrated in three inset pictures (Figs. 8(*a*)–(*c*)), which cover most of the proximity range. Though the figure shows that the resolution of the material loading in terms of C_p is less than 0.001 pF, the effect should still be taken into account over the whole proximity range in order to calculate C_p precisely. C_p can be given in picofarads, considering the material loading effect, as

$$C_p = \left(p\varepsilon_m + q\right)x^{-1} \tag{11}$$

where p=1×10^{-3}, q=4×10^{-3}, x is in mm. Based on the circuit analysis, the resonant frequency of the proximity sensor is

$$f_p = \left[2\pi\sqrt{\left(L - k\sqrt{LL_c}\right)\left(C + C_m + \left(C_c^{-1} + C_g^{-1} + C_p^{-1}\right)^{-1}\right)}\right]^{-1} \tag{12}$$

V. SENSITIVITY

The sensitivity of the proposed sensor was analyzed and quantified for various rotors with a thickness of h_m = 0.5 mm. The sensitivity was calculated in the linear range as the derivative of sensor response with respect to the physical quantity being measured. From Fig. 6(*c*), the angular rotation sensitivity is 4.23 MHz/degree, 3.80 MHz/degree, 3.37 MHz/degree, and 2.73 MHz/degree, using rotors with dielectric constants of 1, 2, 3, and 5, respectively. Fig. 7(*c*) shows that the proximity sensitivity is 11.57 MHz/µm, 9.29 MHz/µm, 7.57 MHz/µm, and 5.53 MHz/µm using rotors with dielectric constants of 1, 2, 3, and 5, respectively.

VI. MEASUREMENT

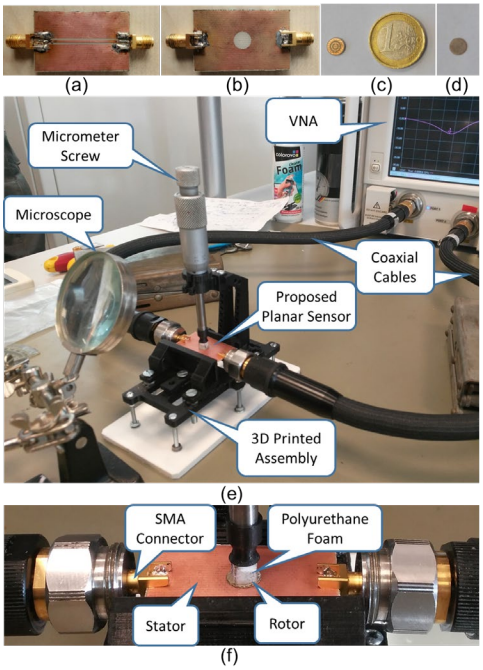

Fig. 9. (*a*) Top layer and (*b*) bottom layer of the fabricated CBCPW based stator; (*c*) top view and (*d*) bottom view of the fabricated rotor; (*e*) the measurement setup, and (*f*) enlarged view of the assembled sensor.

The stator was fabricated on a 0.5-mm-thick RF-35 substrate using standard photolithography techniques. The picture of the top and bottom layers of the fabricated CBCPW based stator is provided in Figs. 9(a) and (b). The rotor was fabricated on TLY-5 (ε_s = 2.2, tan δ = 0.0009) and Taconic RF-35 substrates. The top and bottom views of the fabricated rotor is given in Figs. 9(c) and (d), respectively. A support fixture made of Acrylonitrile Butadiene Styrene (ABS) was realized by additive manufacturing to hold the stator and rotor components in perfect alignment, which is essential to precisely measure angular rotation and proximity. A test fixture was assembled from ABS using a micrometer screw gauge with two degrees of freedom in the vertical direction and rotational movement around the axis. The resolution of the micrometer screw used in the experiment is 0.01 mm, the range of measurement is 0 to 25 mm, and the accuracy of the micrometer is ±10 µm. A microscopic lens was used for manual alignment and taking readings of angular rotation and proximity data. Two subminiature version A (SMA) connectors were mounted on the two ports of the sensor and connected to the vector network analyzer using coaxial cables. The setup for measuring angular rotation and proximity is shown in Fig. 9(d), whereas a detailed enlarged view of the assembled sensor is presented in Fig. 9(e). For uniformity, this section is divided into two subsections dealing with the measurement of angular rotation and the measurement of proximity.

A. Measurement of Angular Rotation

In measuring angular rotation, vertical translation of the rotor is prevented and the center of the rotor is aligned, while firm contact is made with the geometric center of the stator. Only rotational movement around the axis of the rotor is allowed. The angle of rotation of the stator was varied from 0° to 90° in 11 steps. The transmission coefficients were recorded and the resonant frequency corresponding to the angular displacement was measured. The results are plotted in Fig. 10, which also includes data simulated using full-wave FEM code to imitate the real measurement situation—i.e., the stator with SMA connectors and the rotor connected to the axis of the micrometer screw gauge using 5-mm-thick polymethacrylimide (PMI) structural foam. This PMI foam, also referred to as Rohacell, has air-like dielectric properties (dielectric constant 1.07 and loss tangent 0.002 at 5 GHz) and provides the required mechanical strength for rotation and fair isolation between the rotor and the metallic support from the micrometer screw gauge. To verify the theoretical approach described in Section III, the data obtained using (9) are also plotted in Fig. 10.

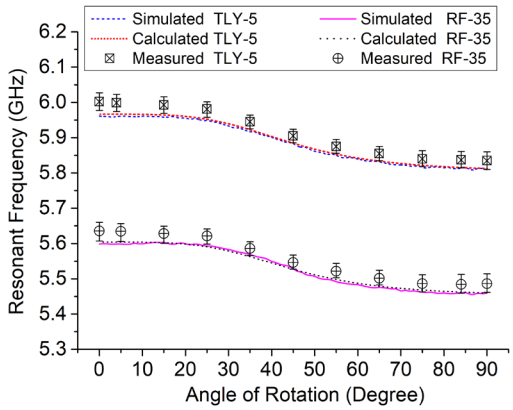

Fig. 10. Measurement of angle of rotation using the microwave sensor.

B. Measurement of Proximity

In measuring proximity, angular rotation around the rotor's axis is prevented and the center of the rotor is aligned with the geometric center of the stator. Vertical movement along the axis of the rotor is allowed. The vertical displacement of the stator was varied from 0 mm to 2 mm in 24 steps. The

transmission coefficients were recorded and the resonant frequencies corresponding to the proximity were measured. The proximity results are plotted in Fig. 11 with simulated data imitating real conditions, as explained previously. To verify the theoretical approach described in Section IV, the data obtained from (12) are also plotted in Fig. 11.

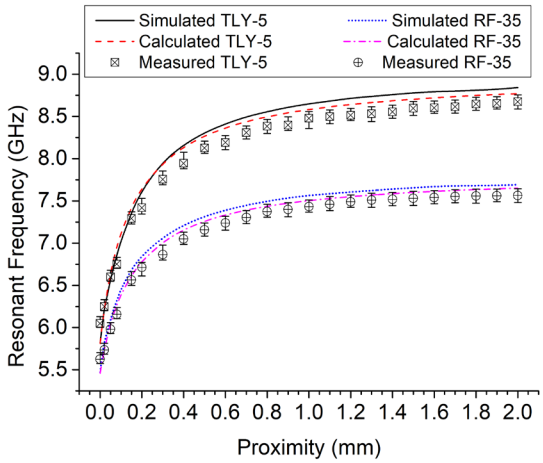

Fig. 11. Measurement of proximity using the microwave sensor.

VII. DISCUSSION

In Figs. 10 and 11, the good match between the calculated and simulated data, obtained numerically by emulating real conditions, validates the newly developed formulae (9) and (12) for measuring respectively the angular displacement and proximity with the sensor. The angular displacement and proximity measurements were repeated several times, and the mean values are plotted with error bars in Figs. 10 and 11. In Fig. 10, the intrinsic air gap of a few micrometers between the rotor and the stator may explain the value being higher than the corresponding simulated or calculated data; however, the values are in good agreement. From Fig. 11, it can be observed that the measured data closely follow the simulated and calculated data. The standard deviation in the angular rotation and proximity measurements were 0.02 MHz and 0.08 MHz, respectively. From Figs. 10 and 11, the performance of the sensor was found to be linear from 30° to 60° when measuring angular rotation and up to 200 µm when measuring proximity. The angular rotation measurement sensitivity was calculated from the slope of the curve in the linear region to be 3.18 MHz/degree and 2.97 MHz/degree using the rotors with TLY-5 and RF-35 dielectric pucks, respectively. The sensitivity of proximity measurement in the linear range of operation was found to be 7.85 MHz/µm and 5.87 MHz/µm using the TLY-5 and RF-35 dielectric pucks, respectively. The angular rotation measurement shows that the BW of the proposed sensor is 167 MHz and 149 MHz using the TLY-5 and RF-35 rotors, respectively. Fig. 10 shows that the bands corresponding to TLY-5 and RF-35 rotors were well isolated at 367 MHz, which demonstrates the band selectivity of the sensor. Unlike the almost constant band isolation in angular rotation, the band isolation measured for proximity sensing was found to vary nonlinearly from 379 MHz to 1.11 GHz over the proximity range. From Fig. 11, the maximum frequency sweep is 2.625 GHz and 1.94 GHz, using TLY-5 and RF-35 rotors, respectively.

A. Enhancing the Dynamic Range of Rotation

The primary purpose of the proposed sensor is to provide a unified scheme for the measurement of rotation and proximity; however, the present configuration offers angular rotation in a limited range of 0°-90°. It is mainly due to the presence of two symmetry planes in the angular span of 180°; the first symmetry plane is along the y-axis at $\theta = 0°$, and the second symmetry plane is along the x-axis at $\theta = 90°$, as shown in Fig. 1(a). The dynamic range of the angular rotation can be increased in a number of ways, a few of them are suggested here.

The idea of independent rotation of both the rings of CSRR offers an extended range of angular rotation from 90° to 180°. The extension of dynamic range is due to the reduction of the number of symmetry planes from 2 to 1 in the angular span of 180°; the only symmetry plane is along the x-axis. Out of the two cases, one particular case is discussed when the outer ring is fixed, and the inner ring is rotated. The schematic and the results are shown in Figs. 12(a) and (b), respectively. From Figs. 2(c) and 12(b), it can be noticed that the dynamic and linear ranges of operation are increased from 90° to 180° and from 30°-60° to 30°-150°, respectively. Another way to enhance the output dynamic range of the proposed sensor for detecting the rotation is to exploit the asymmetric properties of the scattering (S) parameters. The magnitude profile (resonant frequency, quality factor) of the sensor is an even function of rotation angle; however, this does not apply to the phase response. Considering the phase response of the two-port S parameters, the dynamic range of the sensor can be increased from 90° to 180°. The dynamic range can also be extended by wisely choosing the type of stator and rotor. A typical example of enhancing the dynamic and linear ranges of operation are presented in [16].

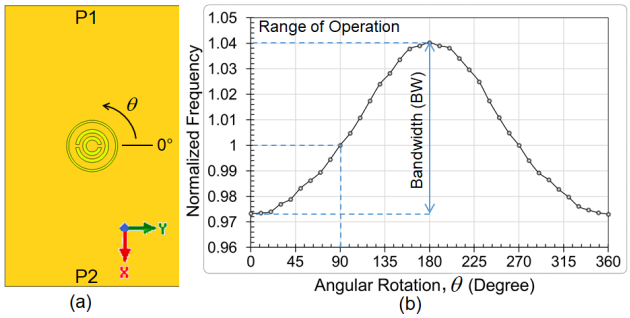

(a) (b)

Fig. 12. Rotation of inner ring to extend the dynamic and linear ranges of operation, and (b) variation of normalized resonant frequency with rotation.

B. Converting Output Parameters to Voltage/Current

For making the cost-effective, practical angular rotation and proximity sensor, it is essential to change the measurement technology of the proposed sensor from the resonant frequency to either voltage or current. The electronic equipment required to process the microwave signal (in the frequency domain) into voltage waveform (in the time domain) is discussed in [12], [14]-[15]. A general representation of extracting the envelope of the modulated

signal due to rotation and proximity measurement in terms of voltage is shown in Fig. 13. The function generator sinusoidal output close to the resonant frequency of the proposed sensor propagates through the planar microwave sensor, which is directed to the rectifier/envelope detector using a circulator. The circulator is used to isolates the sensor from the rectifier to avoid signal interference due to impedance mismatch. For making such a sensing system compatible with the planar technology, a magnetless isolator, as described in [32], can be effectively used. The output voltage waveform in the time domain can be visualized in the oscilloscope.

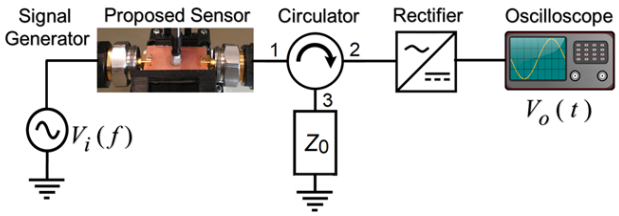

Fig. 13. A general schematic to extract the envelope of the modulated signal due to rotation and proximity measurement

In the presence of resistive loss, it may be possible that voltage signal in a parallel circuit varies from one node to the other node, while the magnitude of current remains the same throughout the series circuit. To represent the rectified voltage in terms of the current, additional circuitry, e.g., an op-amp with negative feedback may be required.

C. Measurement of Unknown Rotation or Proximity

The simultaneous measurement of unknown rotation and proximity from the measured resonant frequency is not possible with the proposed scheme. It is mainly due to two unknowns depending on a single measurable quantity; therefore, uniqueness is not guaranteed. However, the technique can be extended to measure the detection of rotation or proximity, one at a time, in a very effective way. It is a two-step process. In the first step, the type of movement, either rotation or proximity, is identified. The identification of the type of movement rotation or proximity is possible due to the uniqueness of the resonance profile. From Figs. 2(c), and 7(d), it can be easily identified that rotation provides a periodic change in the resonant frequency with a period of 180º, whereas the proximity provides monotonic linear behavior. After processing the signal, as explained in Fig. 13, the angular velocity can be calculated from the period of the envelope signal, recorded by the oscilloscope. One full rotation provides quite a limited BW (maximum 400 MHz) in the resonant frequency, whereas the proximity has broader BW and higher sensitivity than rotation. Once the type of movement is identified, equations (9) or (12) can be used to get the precise value of rotation and the proximity.

D. State of Art of Rotation and Proximity Sensor

For making a fair comparison of the proposed sensor with the sensors available in the literature, the state of the art of the rotation and proximity sensor is presented in Table II. The qualitative comparison among various sensors is made on the basis of the technology, adaptability, and sensing type, whereas the quantitate comparison is performed on dynamic range, sensitivity, sampling, and accuracy. The sensitivity for measuring rotation angle (in degrees) is presented in terms of dB/º and MHz/º, while the sensitivity for measuring proximity is provided in MHz/µm. Since the sampling rate is a major limiting factor for the infrared and ultrasonic sensors, it is given in ms, and the accuracy of proximity is provided in ± mm. From Table II, it can be noted that the proposed sensor bears an impressive specification among the rotation and proximity sensors.

TABLE II. STATE OF THE ART OF ANGULAR DISPLACEMENT SENSORS AND PROXIMITY SENSOR

Ref.	Technology/ Stator: Rotor	Dynamic Range	Adaptability	Proximity Sensing	Sensitivity/ Sampling/ Accuracy	
					Rotation	Proximity
[21]	Microwave/ CPW: SRR	0°-90°	X	X	0.26 dB/º	---
[25]	Microwave/ Microstrip: U-type	0° to 180°	X	X	1.81 MHz/º	---
[26]	Microwave/ CPW: Horn-type	0° to 8°	X	X	1.75 dB/º	---
[27]	Microwave/ Microstrip: CSRR-RF35	0º to 90º	✓ (Freq. Band)	X	1.65 MHz/º	---
[16]	Infrared/ Pulsed mode	(Fixed) 10 cm	X	✓	---	150 ms ---
[18]	Ultrasonic Sensor	3-100 cm	X	✓	---	1 ms ±1 mm
[19]	Fiber Optic Sensor	1 mm	X	✓	---	± $3x10^{-5}$ mm
This work	Microwave/ CBCPW: CSRR-TLY5 CSRR-RF35	0° to 90° and 0 to 2 mm	✓ (Freq. Band Selection)	✓	3.18 MHz/º 2.97 MHz/º	7.85 MHz/µm 5.87 MHz/µm

VIII. CONCLUSION

This paper presented the design, fabrication, and testing of a planar microwave sensor for measuring angular displacement and proximity. It was observed that the sensor can effectively measure both of these physical quantities, which are crucial in the automation industry. The operating frequency range can be selected using several rotors, keeping diameter unchanged while altering the material loading. The prototype is easy to fabricate and assemble, is lightweight, and sufficiently sensitive to measure the angle of rotation in degrees and proximity in micrometers. The formulae proposed in this work were quite accurate for calculating the angular rotation and proximity. The sensor has potential applications in the robotic, industrial, and automotive fields for the calibration and control of errors.

REFERENCES

[1] J. Józwik, *Experimental methods of error identification in CNC machine tool operation*, Lublin University of Technology, 978-83-7947-312-0, 2018.

[2] R Ramesh, M. A. Mannan and A. N Poo, "Error compensation in machine tools — a review: Part I: geometric, cutting-force induced and fixture-dependent errors," *Int. J. Mach. Tool. Manu.*, vol. 40, no. 9, pp. 1235-1256, 2000.

[3] A. Levy, "Multilayer printed circuit interconnection techniques," *IEEE Trans. Compon. Packag. Technol.*, vol. 8, no. 1, pp. 16-20, April 1964.

[4] V. N. Rayapatii and B. Kaminska, "Performance analysis of multilayer interconnections for megabit static random access memory chip," *IEEE Trans. Components Hybrids Manuf. Technol.*, vol. 16, no. 5, pp. 469-477, Aug. 1993.

[5] N. Anandan and B. George, "A wide-range capacitive sensor for linear and angular displacement measurement," *IEEE Trans. Ind. Electron*., vol. 64, no. 7, pp. 5728-5737, 2017.

[6] T. A. Tameh, M. Sawan and R. Kashyap, "Smart integrated optical rotation sensor incorporating a fly-by-wire control system," *IEEE Trans. Ind. Electron*., vol. 65, no. 8, pp. 6505-6514, Aug. 2018.

[7] Z. Zhang, F. Ni, Y. Dong, C. Guo, M. Jin and H. Liu, "A novel absolute magnetic rotary sensor," *IEEE Trans. Ind. Electron*., vol. 62, no. 7, pp. 4408-4419, 2015.

[8] P. Luo, Q. Tang and H. Jing, "Optimal design of angular displacement sensor with shared magnetic field based on the magnetic equivalent loop method," *Sensors*, vol. 19, no. 9, May 2019.

[9] S. R. Khan and M. P. Y. Desmulliez, "Implementation of a dual wireless power transfer and rotation monitoring system for prosthetic hands," *IEEE Access*, vol. 7, pp. 107616-107625, 2019.

[10] J. Deak and I. Jin, "High-field tunneling magnetoresistive angle sensor," *IEEE Trans. Magn*., vol. 55, no. 10, pp. 1-4, Oct. 2019, Art no. 6700104.

[11] Z. Chen and R. C. Luo, "Design and implementation of capacitive proximity sensor using microelectromechanical systems technology," *IEEE Trans. Ind. Electron.*, vol. 45, no. 6, pp. 886-894, Dec. 1998.

[12] J. Won, H. Ryu, T. Delbruck, J. H. Lee and J. Hu, "Proximity sensing based on a dynamic vision sensor for mobile devices," *IEEE Trans. Ind. Electron*., vol. 62, no. 1, pp. 536-544, Jan. 2015.

[13] Z. Xu, R. Wang, X. Yue, T. Liu, C. Chen and S. Fang, "FaceME: face-to-machine proximity estimation based on RSSI difference for mobile industrial human–machine interaction," *IEEE Trans Ind. Informat.*, vol. 14, no. 8, pp. 3547-3558, Aug. 2018.

[14] Y. Kim *et. al.*, "Developing accurate long-distance 6-DOF motion detection with one-dimensional laser sensors: Three-beam detection system," *IEEE Trans. Ind. Electron.*, vol. 60, no. 8, pp. 3386-3395, 2012.

[15] X. Lü et al., "A novel proximity sensor based on parallel plate capacitance," *IEEE Sensors J.*, vol. 18, no. 17, pp. 7015-7022, Sept.1, 2018.

[16] E. Chen *et al*., "Polymer infrared proximity sensor array," *IEEE Trans. Electron Devices*, vol. 58, no. 4, pp. 1215-1220, April 2011.

[17] C. Canali, G. Cicco, B. Morten, M. Prudenziati and A. Taroniet, "A temperature compensated ultrasonic sensor operating in air for distance and proximity measurements," *IEEE Trans. Ind. Electron.*, vol. 4, pp. 336-341, 1982.

[18] B. K. Kim and Ki-Nam Joo, "A multi-channel fiber optic proximity sensor," *Meas. Sci. Technol*., vol. 27, no. 3, 2016.

[19] S. Fericean, A. Dorneich, R. Droxler and D. Krater, "Development of a microwave proximity sensor for industrial applications," *IEEE Sensors J.*, vol. 9, no. 7, pp. 870-876, July 2009.

[20] J. Basseri and M. Joodaki, "An angular displacement sensor with a curved two-metal-layer CPW loaded by an EBG structure," *IEEE Sensors J.*, vol. 18, no. 6, pp. 2335-2341, March, 15 2018.

[21] J. Naqui and F. Martín, "Transmission lines loaded with bisymmetric resonators and their application to angular displacement and velocity sensors," *IEEE Trans. Microw. Theory Techn.*, vol. 61, no. 12, pp. 4700-4713, Dec. 2013.

[22] J. Naqui and F. Martín, "Angular displacement and velocity sensors based on electric-LC (ELC) loaded microstrip lines," *IEEE Sensors J.*, vol. 14, no. 4, pp. 939-940, April 2014.

[23] C. Herrojo, J. Mata-Contreras, F. Paredes and F. Martín, "Microwave encoders for chipless RFID and angular velocity sensors based on S-shaped split-ring resonators," *IEEE Sensors J.*, vol. 17, no. 15, pp. 4805-4813, Aug.1, 2017.

[24] J. Mata-Contreras, C. Herrojo and F. Martín, "Application of split-ring resonator (SRR) loaded transmission lines to the design of angular displacement and velocity sensors for space applications," *IEEE Trans. Microw. Theory Techn.*, vol. 65, no. 11, pp. 4450-4460, Nov. 2017.

[25] A. Ebrahimi, W. Withayachumnankul, S. F. Al-Sarawi and D. Abbott, "Metamaterial-inspired rotation sensor with wide dynamic range," *IEEE Sensors J.*, vol. 14, no. 8, pp. 2609-2614, Aug. 2014.

[26] A. K. Horestani, D. Abbott and C. Fumeaux, "Rotation sensor based on horn-shaped split-ring resonator," *IEEE Sensors J.*, vol. 13, no. 8, pp. 3014-3015, Aug. 2013.

[27] A. K. Jha, N. Delmonte, A. Lamecki, M. Mrozowski and M. Bozzi, "Design of microwave-based angular displacement sensor," *IEEE Microwave and Wireless Components Letters*, vol. 29, no. 4, pp. 306-308, April 2019.

[28] V. Sipal, A. Z. Narbudowicz and M. J. Ammann, "Contactless measurement of angular velocity using circularly polarized antennas," *IEEE Sensors J.*, vol. 15, no. 6, pp. 3459-3466, June 2015.

[29] J.Naqui, M. Durán-Sindreu, and F. Martín, "Modeling split-ring resonator (SRR) and complementary split-ring resonator (CSRR) loaded transmission lines exhibiting cross-polarization effects," *IEEE Antennas Wireless Propag. Lett.*, vol. 12, pp. 178-181, 2013.

[30] D. Halliday, R. Resnick and J. Walker, *Fundamentals of physics*, John Wiley & Sons, 2013.

[31] R. N. Simons, *Coplanar waveguide circuits, components, and systems*, vol. 165. John Wiley & Sons, 2004.

[32] T. Kodera, D. L. Sounas, and C. Caloz, "Magnetless nonreciprocal metamaterial (MNM) technology: Application to microwave components," *IEEE Trans. Microw. Theory Techn.*, vol. 61, no. 3, pp. 1030-1042, 2013.

Abhishek K Jha (S'14–M'17) received Ph.D. degree in RF and Microwaves from IIT Kanpur, India in 2017. He was a Post-Doctoral Research Fellow with the Institute of Photonics and Electronics, Prague, Czechia. In 2018, he joined the Department of Microwave and Antenna Engineering, Gdańsk University of Technology, Poland as an Assistant Professor. He has authored or coauthored more than 40 articles in peer-reviewed international journals and conference proceedings. His current research interests include the numerical analysis and design of novel microwave circuits and waveguide components, development of RF & microwave sensors for nondestructive testing and measurements of intrinsic and physical properties.

Adam Lamecki (M'09–SM'16) received the Ph.D. and D.Sc. degrees in microwave engineering from the Gdańsk University of Technology (GUT), Gdańsk, Poland, in 2007 and 2019, respectively. In 2007, he co-founded a spin-off company EM Invent, that develops an electromagnetic filed simulator InventSim, where he serves as the CTO. Since 2019, he is Associate Professor with the Department of Microwave and Antenna Engineering at GUT. His research interests include surrogate models and their application in the CAD of microwave devices, computational electromagnetics mainly focused on the finite element method and filter design and optimization techniques.

Michal Mrozowski (S'88–M'90–SM'02–F'08) received the M.Sc. and Ph.D. degrees (Hons.) from the Gdańsk University of Technology, in 1983 and 1990, respectively. He joined the Faculty of Electronics, Gdańsk University of Technology, in 1986, where he is currently a Full Professor, the Head of the Department of Microwave and Antenna Engineering. His current research interests include computational electromagnetics, the CAD of microwave devices, filter and sensor design, and optimization techniques.

Maurizio Bozzi (S'98–M'01–SM'12–F'18) received the Ph.D. degree in electronics and computer science from the University of Pavia, Pavia, Italy, in 2000. In 2002, he joined the Department of Electronics, University of Pavia, where he is currently a full professor of electromagnetic fields. He has authored or co-authored more than 130 journal papers and 300 conference papers. He co-edited the book *Periodic Structures* (Research Signpost, 2006) and co-authored the book *Microstrip Lines and Slotlines* (Artech House, 2013). His main research interests concern the computational electromagnetics, the substrate integrated waveguide technology, and the use of novel materials and fabrication technologies for microwave circuits.